Available online at www.sciencedirect.com

ScienceDirect

Procedia Engineering 197 (2017) 185 – 195

Procedia Engineering

www.elsevier.com/locate/procedia

DYMAT 23rd Technical Meeting

Dynamic Fracture of Ductile Materials

# Ductile Fracture of Steel Sheets under Dynamic Membrane Loading

Gaute Gruben[a,c,*], David Morin[b,c], Magnus Langseth[b,c] and Odd S. Hopperstad[b,c]

[a]*SINTEF Materials and Chemistry, Rich. Birkelands vei 2B, NO-7491 Trondheim*
[b]*Department of Structural Engineering, NTNU, Norwegian University of Science and Technology, NO-7491 Trondheim, Norway*
[c]*Centre for Advanced Structural Analysis, Centre for Research-based Innovation (CRI), NTNU, Norwegian University of Science and Technology, NO-7491 Trondheim, Norway*

**Abstract**

Failure prediction assessment is conducted based on validated finite element simulations of impact tests performed on 1.8 mm dual-phase and 1.0 mm martensitic steel sheets. The sheets were clamped between two steel rings and subjected to lateral loading by a punch with a hemispherical nose. Three different specimen geometries were applied. These were chosen to provide membrane loading in stress states near uniaxial tension, plane-strain tension and equi-biaxial tension. Thus, the most important stress states that may occur for thin sheets in an impact situation are covered. Finite element simulations of the impact tests are run with the nonlinear code LS-DYNA. The plastic behaviour of the materials is modelled using the Hershey yield function in combination with the associated flow rule and isotropic hardening. The specimens are discretized by shell elements, thus imposing a state of plane stress. Three different approaches for modelling ductile failure are evaluated by comparing the experimental and simulated force-displacement curves from the experiments on the two steel materials.

*Keywords:* Ductile Failure; Strain Localization; Finite Element Analysis

## 1. Introduction

In many structural applications membrane loading may lead to failure. Some examples are car collisions, ship-ship collisions, ship grounding [1, 2] and metal forming [3-6]. Fracture from this type of loading is often preceded by strain localization. In most instances, the sheet exhibits local necking [7] which occurs on a length scale comparable to the

* Corresponding author. Tel.:+47 48 28 22 91.
*E-mail address:gaute.gruben@sintef.no*


Peer-review under responsibility of the scientific committee of the International Conference on Dynamic Fracture of Ductile Materials
doi:10.1016/j.proeng.2017.08.095

sheet thickness, before strain localization between microvoids results in void coalescence and final fracture [8, 9]. In some cases, however, onset of fracture is not preceded by local necking, but by shear banding [10] which occurs on a length scale of a few micrometres. The latter phenomenon is sometimes seen in equi-biaxial tension, see e.g. [11]. In general, onset of shear banding cannot be predicted by a plasticity model unless special features of the constitutive model are introduced such as material softening or a vertex on the yield surface [12].

Fracture preceded by microvoid nucleation, growth and coalescence is strongly affected by the hydrostatic stress state; increased pressure restricts the growth of the microvoids and leads to a more ductile behaviour [13]. The hydrostatic stress state is commonly described by the stress triaxiality parameter $\sigma^* = \sigma_m / \sigma_{VM}$, where $\sigma_m$ is the mean stress and $\sigma_{VM}$ is the von Mises equivalent stress. Over the last decade, several studies indicate that the deviatoric stress state also influences the ductility of metal sheet [14-21]. Several parameters can be applied to evaluate the deviatoric stress state, such as the Lode parameter $\mu$ [22] or the normalized third invariant $\xi$ [23]. However, for a state of plane-stress, which is a good approximation for thin sheets, there is a relation between $\sigma^*$ and the parameter characterizing the deviatoric stress state, e.g. [17]. As a macroscopic measure for the ductility, the equivalent plastic strain at onset of fracture, $p_f$, is often applied, e.g. [24-26]. Accounting for the material state, $p_f$ can be expressed as a function of the stress state parameters $\sigma^*$ and $\mu$ as well as other parameters such as the temperature $T$ and the strain rate $\dot{p}$.

## 2. Experimental programme

The experimental programme is presented in [27], but is briefly repeated here for the readers' convenience.

### *2.1. Materials*

Experiments were conducted on a 1.8 mm thick cold-rolled dual-phase steel sheet, Docol 600DL [28], and on a 1.0 mm thick cold-reduced martensitic steel sheet, Docol 1400M [29]. Uniaxial tensile tests were carried out 0°, 45° and 90° to the rolling direction for both materials. The dual-phase steel displayed initial yielding at ~320 MPa and an ultimate stress of ~620 MPa at an engineering strain of ~0.2, while the martensitic steel displayed initial yielding at ~1200 MPa and an ultimate stress of ~1530 MPa at ~0.028 engineering strain. For both materials, it was found that the Lankford coefficients and the flow stress ratios were close to unity. From cross-section area-reduction measurements, the average strain in the minimum cross-section was estimated to ~0.8 and ~0.4 at fracture for the dual-phase and the martensitic steel, respectively. Tensile testing at elevated strain rates were conducted in a split-Hopkinson bar set-up [30]. When increasing the strain-rate in uniaxial tension from 0.001/s to 100/s, an increase in flow stress of approximately 70 MPa was found for both materials, which implies an increase of 11% for the dual-phase steel and 5% for the martensitic steel.

### *2.2. Punch tests*

Quasi-static and low-velocity punch tests were conducted, using a test rig involving two steel rings for clamping the specimen and an arrangement for monitoring the deformation on the surface of the specimens with cameras. Fig. 1(a) presents a schematic view of the clamping and monitoring system, while Fig. 1(b) shows the specimen geometries, namely S20, S100 and S150. The clamping rings had an inner radius of 75 mm. To measure the out-of-plane deformation, two cameras were employed in the test set-up, see Fig. 1(c) and (d), and a mirror was positioned inside a cylinder with cut-outs to enable the camera recordings, as indicated in Fig. 1(a) and (c). The specimen surface facing the mirror was spray-painted with a speckle pattern to provide optical measurements that could be post-processed in an in-house digital image correlation (DIC) software [31]. Loading was provided by a punch with a hemispherical nose with radius 50 mm, and a lubricant (Klüber Unimoly C220) was sprayed on the side of the specimen facing the punch to reduce friction. During loading, the S20 geometry invokes uniaxial tension in the gauge region of the

specimen, while the S100 and the S150 geometries provide a stress-state near plane-strain tension and equi-biaxial tension, respectively.

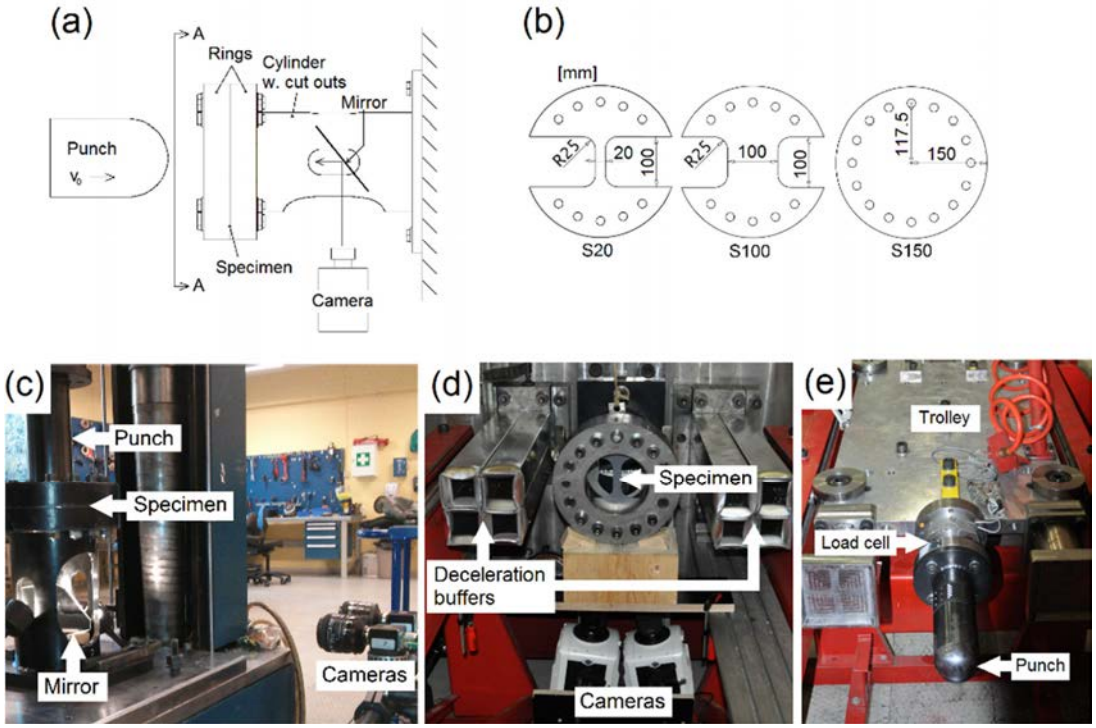


Fig. 1 (a) Schematic view of experimental set-up, (b) specimen geometry, (c) set-up for quasi-static testing, (d) set-up for dynamic testing and (e) trolley with load cell and punch.

The quasi-static tests were performed under displacement control at 0.3 mm/s in a hydraulic testing machine with a capacity of 250 kN, see Fig. 1(c). Two duplicate tests were performed per geometry for each material. The force and the cross-head displacement was measured by the testing machine, while two cameras positioned ~1 m from the mirror recorded the tests with a framing rate of 2 Hz for the dual-phase steel and 4 Hz for the martensitic steel. The force-displacement curves from these tests are shown in Fig. 7.

The low-velocity tests were conducted using a pendulum impactor [32], where a trolley equipped with a load cell and the punch, see Fig. 1(e), having a total mass of 417.5 kg, was accelerated to initial velocity $v_0 = 10.5$ m/s before striking the specimen. Three duplicate tests were performed per geometry for each material. The force, $P$, was recorded by the load cell positioned between the punch and the trolley. The force acting between punch and specimen, $F$, the punch velocity, $\dot{u}$, and the punch displacement, $u$, were estimated as

$$F = \left(1 + \frac{M_P}{M_T}\right) P, \quad \dot{u} = v_0 - \int_0^t \frac{P}{M_T} dt, \quad u(t) = \int_0^t \dot{u} dt \tag{1}$$

where $M_T$ = 385 kg is the mass of the trolley and the back-part of the load cell, and $M_P$ = 32.5 kg is the mass of the punch and the front part of the load cell. Fig. 8 shows the force-displacement curves from the low-velocity tests.

## 3. Finite element models

Simulations of the tests were conducted with the nonlinear finite element solver LS-DYNA. The specimens were discretized by Belytschko-Tsay shell elements with an initial characteristic size of 2.5 mm in the gauge region and

five integration points through the thickness following the Gauss-Legendre quadrature. Appropriate boundary conditions were ensured by positioning the specimen between two rigid brackets with distance 0.01 mm larger than the specimen thickness, see Fig. 2(a), and by fixing the outermost nodes of the specimen in the in-plane directions as shown in Fig. 2(b). The punch nose was discretized by hexahedral elements having a characteristic element size of 5 mm. In the quasi-static simulations, loading was enforced by prescribing a displacement of 0.3 mm/s on a node set on the back-side of the punch nose. In the quasi-static analyses, an appropriate amount of mass scaling was used to obtain a reasonable computation time while ensuring negligible kinetic energies. In the models of the dynamic tests, the trolley and the load cell were included, thus ensuring an impacting mass similar to the experimental load, see Fig. 2(c).

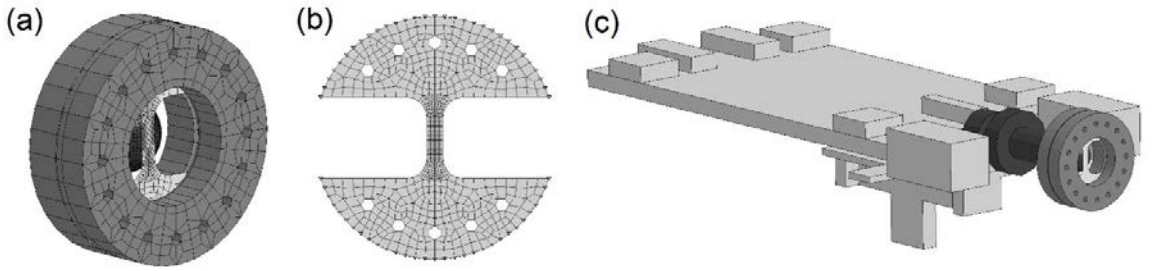


Fig. 2 (a) Mesh of specimen fixed between clamping brackets. (b) Mesh of S20 specimen, where the nodes fixed for in-plane deformations are marked. (c) Geometry of a low-velocity FE model.

### *3.1. Constitutive modelling*

The Hershey yield function [33] with associated flow, isotropic hardening and rate dependence (viscoplasticity) was found appropriate for both materials [27]. The dynamic yield function is given as

$$f = \sigma_{eq} - \sigma_f = 0 \tag{2}$$

where $\sigma_{eq}$ is the equivalent stress and $\sigma_f$ is the flow stress. The equivalent stress is defined from the ordered principal stresses, $\sigma_1 \geq \sigma_2 \geq \sigma_3$, as

$$\sigma_{eq} = \sqrt[m]{\frac{1}{2}\left(\left(\sigma_1 - \sigma_2\right)^m + \left(\sigma_2 - \sigma_3\right)^m + \left(\sigma_1 - \sigma_3\right)^m\right)} \tag{3}$$

where $m$ is an exponent controlling the $J_3$ influence on the yield surface. Logan and Hosford [34] found that $m = 6$ is an appropriate value for BCC materials, and this value was found suitable for the present materials. The flow stress is defined as

$$\sigma_f\left(p, \dot{p}\right) = \left(\sigma_0 + \sum_{i=1}^{3} Q_i\left(1 - \exp\left(-C_i p\right)\right)\right)\left(1 + \frac{\dot{p}}{\dot{p}_0}\right)^c \tag{4}$$

where $\sigma_0$ is the initial yield stress, $Q_i$ and $C_i$ $(i = 1,2,3)$ are parameters governing the work hardening, $\dot{p}$ is the equivalent plastic strain-rate which is power conjugate with the equivalent stress and $p = \int \dot{p}\, dt$ is the equivalent plastic strain. The parameters $c$ and $\dot{p}_0$ control the influence of the strain rate. The material parameters are shown in Tab. 1.

Tab. 1 Material parameters for the two steels [27]

| Material | $\sigma_0$ [MPa] | $Q_1$ [MPa] | $C_1$ | $Q_2$ [MPa] | $C_2$ | $Q_3$ [MPa] | $C_3$ | $\dot{p}_0$ [$s^{-1}$] | $c$ | $m$ |
|---|---|---|---|---|---|---|---|---|---|---|
| 600DL | 317 | 201 | 38.4 | 348 | 5.00 | 6000 | 0.01 | 0.001 | 0.009 | 6.0 |
| 1400M | 1200 | 254 | 774 | 97.0 | 135 | 200 | 6.00 | 0.001 | 0.004 | 6.0 |

### *3.2. Validation*

The force-displacement curves from the low-velocity simulations were obtained in a similar manner as in the experiments by collecting the force acting in the cross section of the load cell and applying Eq. (1). In the quasi-static simulations, the contact force between specimen and punch and the displacement of the rigid punch were collected. The simulated force-displacement curves are generally in good agreement with the experimental curves as shown in Fig. 7 and Fig. 8, and the numerical models are deemed adequate to capture the global response of the tests. The local stress and strain histories at critical locations in the specimen are not metrics used in the validation process; however, the spatial discretization (i.e., 2.5 mm characteristic elements size) and the application of shell elements put restrictions on the accuracy of the local deformation histories. Fig. 3(a) indicates that the applied discretization should be able to capture the diffuse necking phenomenon in the S20 tests, but the local (through thickness) necking occurs on a length scale smaller than the element size, as shown in Fig. 3(b).

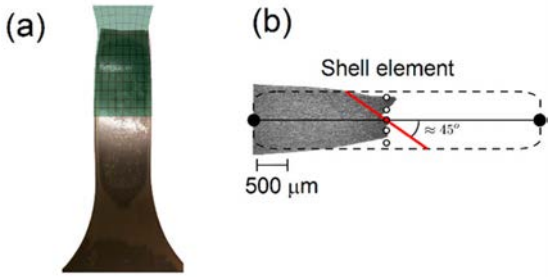


Fig. 3 (a) Illustration shell element size compared to width of the S20 specimen at onset of fracture (Docol 600DL). (b) Comparison of thickness of S20 specimen (1400M) and the shell element.

## 4. Failure criteria

Three failure criteria are assessed in this study through the post-processing of the validated simulations. The first failure criterion, the BWH criterion, aims to predict sheet necking, or strain localization where the sheet thickness is the significant length scale. This criterion does not explicitly take the deformation history into account. The second criterion, the Cockcroft-Latham criterion, is phenomenological and predicts fracture initiation based on damage evolution. The deformation history is accounted for as the predicted damage is accumulating with the equivalent plastic strain. The third criterion is based on strain localization theory and predicts onset of shear banding, i.e., strain localization in bands where the width is a few micrometres. The criterion accounts for the deformation history and estimates the direction of the shear band which rapidly is followed by void coalescence and final fracture. In the following, brief descriptions of the three criteria are given along with details regarding the calibration procedures.

### *4.1. BWH criterion*

The BWH criterion [35] is a stress-based criterion which predicts onset of local necking. The criterion assumes a state of plane stress and is thus adequate for shell elements. In contrast to strain based failure criteria, the stress-based BWH criterion accounts for changes in the load path during deformation, but the criterion is not explicitly history dependent. By defining $\beta$ as the ratio between the minor plastic principal strain increment $d\varepsilon_2^p$ and the major plastic principal strain increment $d\varepsilon_1^p$ in the plane of the sheet, the BWH criterion invoke the Hill criterion for local necking [36] in the regime $-1 < \beta \leq 0$ and the Bressan-Williams criterion [37] for $0 \leq \beta \leq 1$ as

$$\frac{d\sigma_1}{d\varepsilon_1^p} - (1+\beta)\sigma_1 \leq 0 \quad \text{for} \quad -1 < \beta \leq 0 \tag{5}$$

$$\sigma_1 \le \frac{2\tau_c}{\sqrt{1-\left(\frac{\beta}{2+\beta}\right)^2}} \quad \text{for} \quad 0 \le \beta \le 1 \tag{6}$$

where $\tau_c$ is a critical shear stress value defined from the Hill criterion for plane strain ( $\beta = 0$ ). The BWH criterion is determined by the plastic behaviour of the material and needs no additional calibration tests. One limitation of the BWH criterion is that the rate dependence is not included, thus limiting its application to quasi-static analyses.

### *4.2. Cockcroft-Latham criterion*

The Cockcroft-Latham criterion (CL) [38] is a phenomenological fracture criterion defined by

$$W = \int_0^p \max\left(0, \sigma_1\right) dp \le W_C \tag{7}$$

where $W_C$ is the fracture parameter. Fracture occurs when $W$ reaches the critical value $W_C$, and the fracture strain depends on both the stress triaxiality and the Lode parameter. As this criterion involves only one parameter, its calibration can be carried out using one single experiment, for instance a uniaxial tensile test.

### *4.3. Strain localization theory*

The strain localization theory (SLT) predicts onset of shear banding in the material. In the present study, a method based on the imperfection analysis introduced by Rice [10] is applied. Material softening is assumed to occur in local bands where the material is described by a modified version of the Gurson model, where the yield function is given as

$$f = \left(\frac{\sigma_{eq}}{\sigma_M}\right)^2 + 2q_1\omega\cosh\left(\frac{3}{2}q_2\frac{\sigma_m}{\sigma_M}\right) - \left(1+q_1^2\omega^2\right) = 0 \tag{8}$$

where $\sigma_{eq}$ is the equivalent stress as defined by Eq.(3), $\sigma_M$ is the flow stress of the matrix, here equal to $\sigma_f$ defined by Eq.(4), and $\omega$ is the porosity. The parameters $q_1$ and $q_2$ of the Gurson model are taken from Tvergaard [39]: $q_1 = 1.5$ and $q_2 = 1.0$. The imperfection in this study is defined as an initial porosity $\omega_0$ inside the local bands. A similar numerical treatment as proposed in [40] is used with the important difference that viscoplasticity is introduced through the definition of $\sigma_M$. Therefore, the onset of shear banding is not defined by the loss of ellipticity of the constitutive equations of the band material, but when the strain rate inside the band is 50 times larger than the strain rate outside the band.

### *4.4. Calibration and evaluation of the failure criteria*

While the BWH criterion requires no specific calibration, the Cockcroft-Latham (CL) criterion and the strain localization theory (SLT) requires a calibration with at least one experiment. To this end, the CL criterion and the SLT were calibrated from a quasi-static uniaxial tensile test [27]. These calibrations are based on DIC analyses of the quasi-static tensile tests. The local deformations are computed based on a Q4 DIC element [31] which size matches the critical shell elements in the FE models. This element is positioned on the surface of the specimens where the largest deformations were identified, see Fig. 4. Based on the local deformations extracted from the quasi-static tensile tests and assuming a state of plane stress, the local stress histories were recomputed in a stand-alone FORTRAN programme and used later in the strain localization analyses and to calibrate the CL criterion.

By applying the local stress histories onto a set of imperfection bands (in which the Gurson model is employed) the initial porosity was calibrated to obtain failure by shear banding between the two last pictures recorded of the quasi-static tensile test, see Fig. 4(b). This optimisation process led to an initial porosity $\omega_0$ of 0.8 % and 1.1% for the

Docol 600DL and the Docol 1400M, respectively. To obtain an unbiased comparison between the CL criterion and the SLT, the fracture parameter $W_C$ was integrated using Eq. (7) up to the point of shear banding of the strain localization analyses.

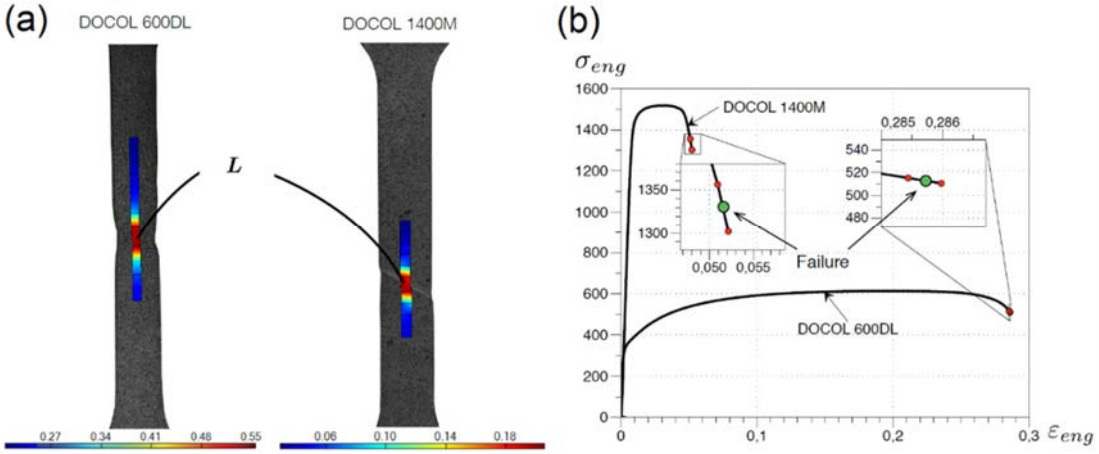


Fig. 4 (a) Last image before fracture in selected tensile tests for the two materials. The elements applied for collecting the velocity gradient are indicated. The contours represent the effective logarithmic strain. (b) Engineering stress-strain curves from the two tests. The red dots represent the points from the two last images, while the green dots are the point defined as the fracture initiation point in the CL and SLT calibrations.

Fig. 5 shows the failure loci defined by the calibrated failure criteria for the dual-phase and the martensitic steels for the range $1/5 \le \sigma^* \le 2/3$. Clearly the BWH criterion generally estimates a lower failure strain than the other two criteria, except in stress-states close to equi-biaxial tension ($\sigma^* = 2/3$). Notably the slope of the fracture locus is similar for the CL criterion and the Hill part of the BWH criterion ($\sigma^* \le \sqrt{3}/3$) for both materials. The SLT curve is closer to the BWH criterion for plane strain tension ($\sigma^* = \sqrt{3}/3$), but fails to predict reasonable failure strains for $\sigma^* < 0.4$ due to the inability of the porous plasticity model to accurately predict void evolution at low stress triaxiality.

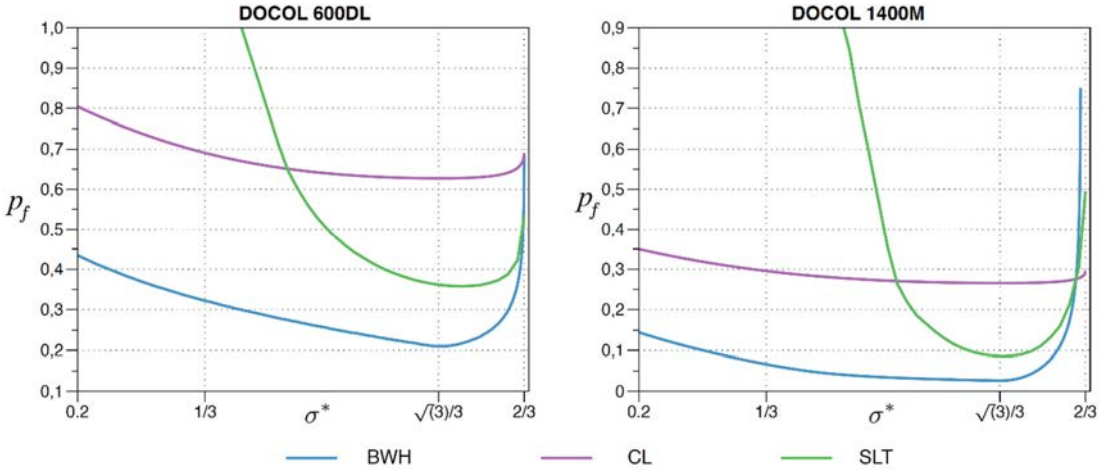


Fig. 5 Failure loci defined by the BWH criterion, the Cockcroft-Latham criterion and the strain-localization theory for the dual-phase (left) and the martensitic (right) steel sheet

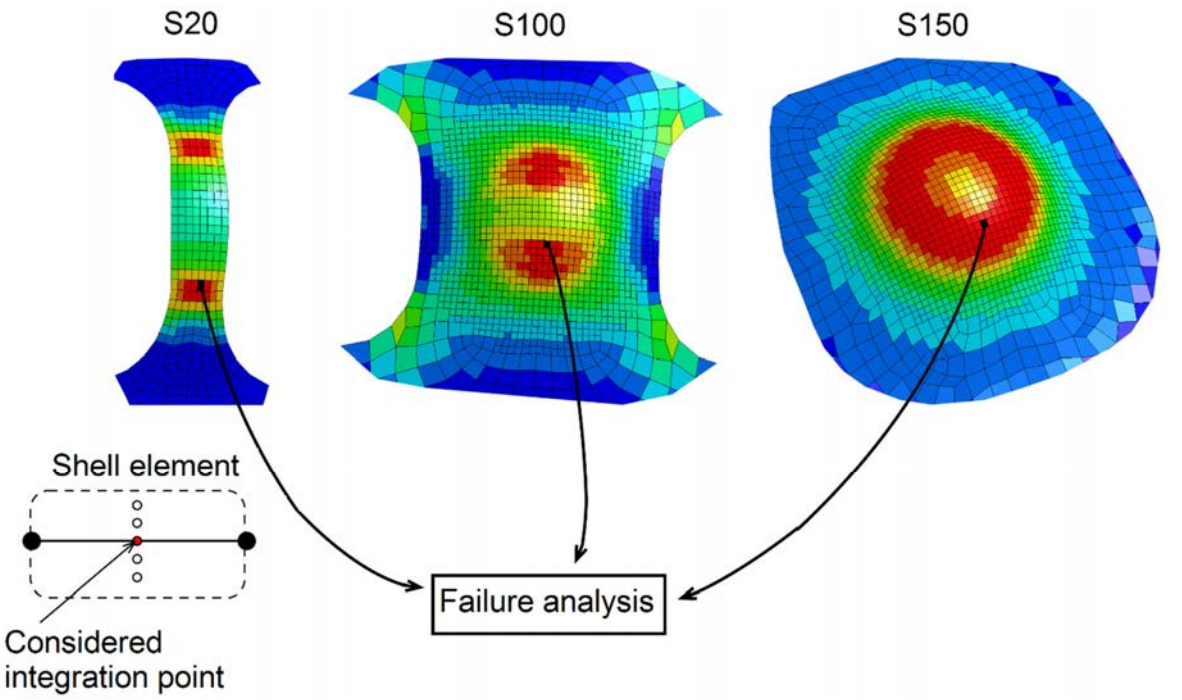


Fig. 6 Position of critical elements in S20, S100 and S150 specimens at the punch displacement corresponding to onset of fracture (from quasi-static Docol 600DL simulation). The position of the integration point considered for collecting the local histories is indicated.

## 5. Results

In each simulation of the punch tests, the element with the largest plastic strain, from now on denoted the critical element, was identified, and the local histories of stress and strain were collected from this element and applied in the failure criteria. As an example, the position of the critical elements in the quasi-static simulations of the dual-phase steel are shown in Fig. 6.

The predicted fracture initiation according to the three criteria for the quasi-static loading case is shown in Fig. 7. In the case of the dual-phase steel, all three criteria give a good estimate of failure. The BWH criterion is somewhat more conservative than the SLT, which again is more conservative than the CL criterion. For the martensitic material, the BWH criterion is conservative for the S20 and S100 tests, which display necking, but non-conservative for the S150 specimen. The latter is likely due to the absence of necking in these experiments and the low work-hardening of this material. The CL criterion and the SLT overestimate the displacement at failure for the S20 specimen, and slightly underestimate the failure in the S150 specimen. The overestimation of failure in the S20 specimen of the Docol 1400M is most likely linked to the finite element model which is not able to capture appropriately the local deformation of the specimen. For the S100 specimen, the CL criterion accurately predicts the displacement at failure, while the SLT analysis is somewhat conservative.

The BWH criterion was not assessed in the low-velocity simulations because the formulation does not account for rate sensitivity. The predicted onset of failure following CL criterion and SLT is shown in Fig. 8. These two criteria display the same trends as in the quasi-static simulations; the CL criterion is somewhat less conservative than the SLT for the dual-phase steel and the S100 specimen of the martensitic material, while the CL criterion is more conservative for the S20 and S150 specimens of the martensitic steel. Compared to the quasi-static assessment, the criteria behave very similar for the dual-phase steel, while they are more conservative for the martensitic steel. This leads to a better prediction of onset of failure in the S20 geometry.

## 6. Concluding remarks

Three failure criteria have been assessed based on data from quasi-static punch tests performed on dual-phase and martensitic steel sheets, and two of the criteria have been assessed on low-velocity impact tests on the same sheet materials. This study shows that the BWH criterion can provide a conservative estimate of ductile failure when the material exhibit significant work-hardening. The Cockcroft-Latham criterion gives, in general, good estimation of the initiation of ductile failure, while having a single parameter and thus a limited calibration cost. The strain localization analyses provide an interesting approach to predict ductile failure, but require that the local stress and strain histories are captured appropriately by the finite element model.

## Acknowledgements

The support from Centre for Advanced Structural Analysis (CASA), Centre for Research-based Innovation (CRI) is highly acknowledged.

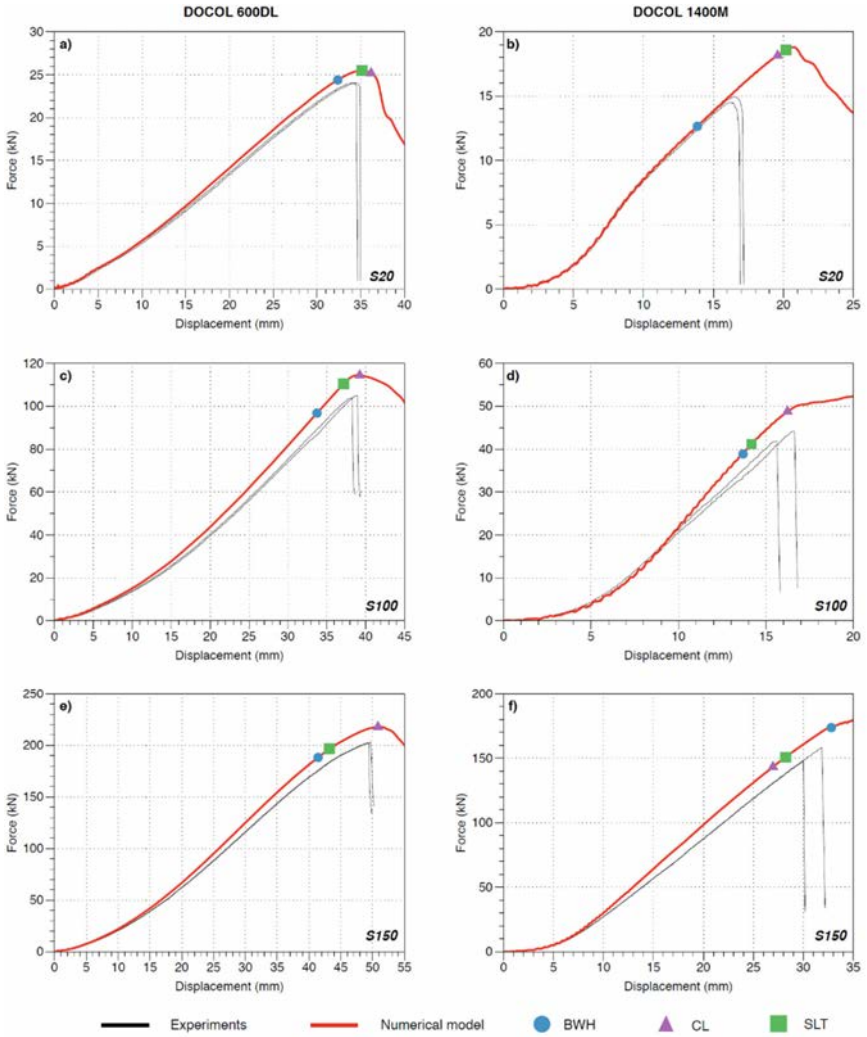


Fig. 7 Results from quasi-static experiments and simulations. The predicted onset of failure is shown for the three failure criteria.

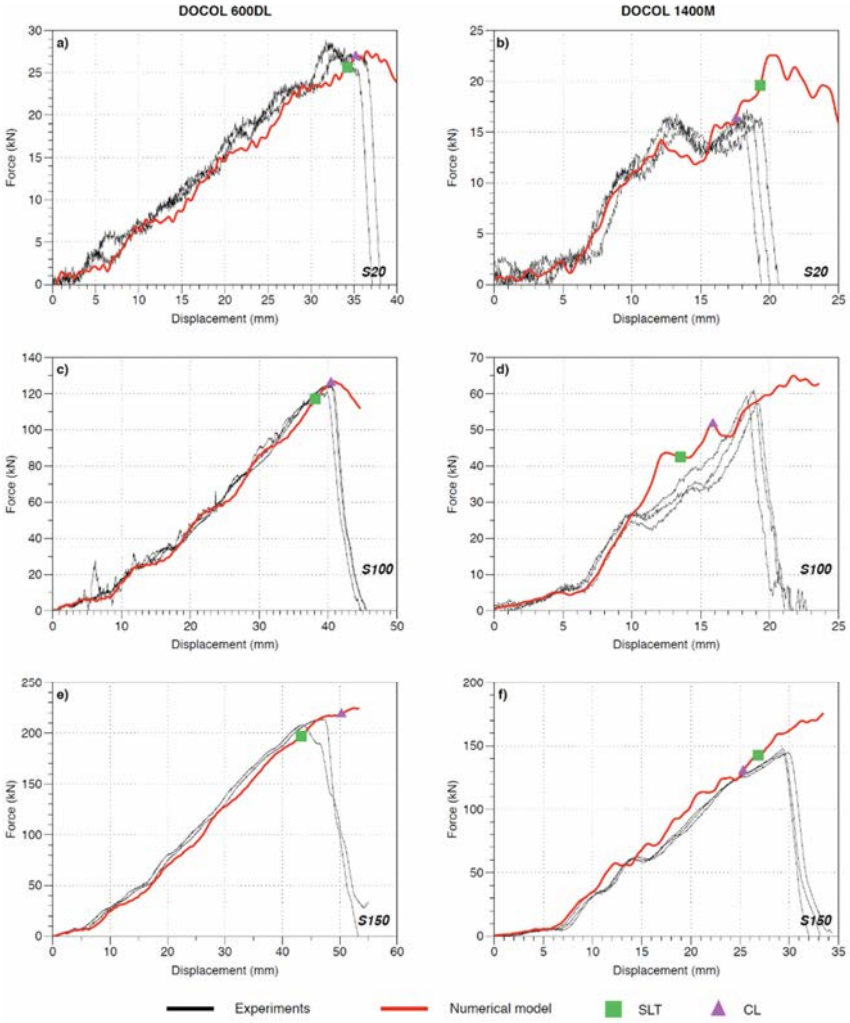


Fig. 8 Force-displacement curves from low-velocity experiments and simulations. The predicted onset of failure is shown for the Cockcroft-Latham (CL) criterion and the strain localization theory (SLT).

## References

[1] Paik, J. K. and Pedersen, P. T. (1996). Modelling of the internal mechanics in ship collisions. Ocean Engineering 23(2): 107-142.
[2] Simonsen, B. C. (1997). Ship grounding on rock—I. Theory. Marine Structures 10(7): 519-562.
[3] Marciniak, Z. and Kuczyński, K. (1967). Limit strains in the processes of stretch-forming sheet metal. International Journal of Mechanical Sciences 9(9): 609-620.
[4] Keeler, S. P. and Backhofen, W. A. (1964). Plastic instability and fracture in sheet streched over rigid punches. ASM Transactions Quarterly 56: 25-48.
[5] Goodwin, G. M. (1968). Application of strain ananlysis to sheet metal forming in the press shop. Report.
[6] Stoughton, T. B. and Yoon, J. W. (2011). A new approach for failure criterion for sheet metals. International Journal of Plasticity 27(3): 440-459.
[7] Martins, P. A. F., Bay, N., Tekkaya, A. E. and Atkins, A. G. (2014). Characterization of fracture loci in metal forming. International Journal of Mechanical Sciences 83: 112-123.
[8] McClintock, F. A. (1968). Criterion for ductile fracture by growth of holes. Journal of applied mechanics 35: 363-371.
[9] Rice, J. R. and Tracey, D. M. (1969). On the ductile enlargement of voids in triaxial stress fields. Journal of the Mechanics and Physics of Solids 17: 201-217.

[10] Rice, J. R. (1977). The localization of plastic deformation. Delft, North-Holland Publishing.
[11] Björklund, O. and Nilsson, L. (2014). Failure characteristics of a dual-phase steel sheet. Journal of Materials Processing Technology 214(6): 1190-1204.
[12] Hutchinson, J. W. and Tvergaard, V. (1981). Shear band formation in plane strain. International Journal of Solids and Structures 17(5): 451-470.
[13] Bridgman, P. W. (1952). Studies in large plastic flow and fracture: with special emphasis on the effects of hydrostatic pressure. Cambridge, Mass., Harvard Univ. Press.
[14] Bao, Y. and Wierzbicki, T. (2004). On fracture locus in the equivalent strain and stress triaxiality space. International Journal of Mechanical Sciences 46: 81-98.
[15] Barsoum, I. and Faleskog, J. (2007). Rupture mechanisms in combined tension and shear—Experiments. International Journal of Solids and Structures 44(6): 1768-1786.
[16] Mohr, D. and Ebnoether, F. (2009). Plasticity and fracture of martensitic boron steel under plane stress conditions. International Journal of Solids and Structures 46(20): 3535-3547.
[17] Gruben, G., Vysochinskiy, D., Coudert, T., Reyes, A. and Lademo, O.-G. (2013). Determination of ductile fracture parameters of a dual-phase steel by optical measurements. Strain 49(3): 221-232.
[18] Roth, C. C. and Mohr, D. (2016). Ductile fracture experiments with locally proportional loading histories. International Journal of Plasticity 79: 328-354.
[19] Gao, X. and Kim, J. (2006). Modeling of ductile fracture : Significance of void coalescence. International Journal of Solids and Structures 43: 17.
[20] Barsoum, I. and Faleskog, J. (2011). Micromechanical analysis on the influence of the Lode parameter on void growth and coalescence. International Journal of Solids and Structures 48(6): 925-938.
[21] Dunand, M. and Mohr, D. (2014). Effect of Lode parameter on plastic flow localization after proportional loading at low stress triaxialities. Journal of the Mechanics and Physics of Solids 66: 133-153.
[22] Lode, W. (1926). Versuche über den Einfluß der mittleren Hauptspannung auf das Fließen der Metalle Eisen, Kupfer und Nickel. Zeitschrift für Physik A Hadrons and Nuclei 36: 913-939.
[23] Bai, Y. and Wierzbicki, T. (2008). A new model of metal plasticity and fracture with pressure and Lode dependence. International Journal of Plasticity 24(6): 1071-1096.
[24] Hancock, J. W. and Mackenzie, A. C. (1976). On the mechanisms of ductile failure in high-strength steels subjected to multi-axial stress-states. Journal of the Mechanics and Physics of Solids 24(2-3): 147-169.
[25] Johnson, G. R. and Cook, W. H. (1985). Fracture characteristics of three metals subjected to various strains, strain rates, temperatures and pressures. Engineering Fracture Mechanics 21(1): 31-48.
[26] Gruben, G., Fagerholt, E., Hopperstad, O. S. and Børvik, T. (2011). Fracture characteristics of a cold-rolled dual-phase steel European Journal of Mechanics - A/Solids 30: 204-218.
[27] Gruben, G., Langseth, M., Fagerholt, E. and Hopperstad, O. S. (2016). Low-velocity impact on high-strength steel sheets: An experimental and numerical study. International Journal of Impact Engineering 88: 153-171.
[28] SSAB. "Docol 600DL." Retrieved 05.01, 2014, from http://www.ssab.com/en/Brands/Docol1/Products/Docol-600-DL/.
[29] SSAB. "Docol 1400M." Retrieved 05.02, 2014, from http://www.ssab.com/en/Brands/Docol1/Products/Docol-1400-M/.
[30] Chen, Y., Clausen, A. H., Hopperstad, O. S. and Langseth, M. (2011). Application of a split-Hopkinson tension bar in a mutual assessment of experimental tests and numerical predictions. International Journal of Impact Engineering 38(10): 824-836.
[31] Fagerholt, E., Borvik, T. and Hopperstad, O. S. (2013). Measuring discontinuous displacement fields in cracked specimens using digital image correlation with mesh adaptation and crack-path optimization. Optics and Lasers in Engineering 51(3): 299-310.
[32] Hanssen, A. G., Auestad, T., Tryland, T. and Langseth, M. (2003). The kicking machine: A device for impact testing of structural components. International Journal of Crashworthiness 8(4): 385-392.
[33] Hershey, A. V. (1954). The Plasticity of an Isotropic Aggregate of Anisotropic Face-Centered Cubic Crystals. Journal Applied Mechanics 76: 241-249.
[34] Logan, R. and Hosford, W. F. (1980). Upper-bound anisotropic yield locus calculations assuming -pencil glide. International Journal of Mechanical Sciences 22: 419-430.
[35] Alsos, H. S., Hopperstad, O. S., Törnqvist, R. and Amdahl, J. (2008). Analytical and numerical analysis of sheet metal instability using a stress based criterion. International Journal of Solids and Structures 45(7–8): 2042-2055.
[36] Hill, R. (1952). On discontinuous plastic states, with special reference to localized necking in thin sheets. Journal of the Mechanics and Physics of Solids 1(1): 19-30.
[37] Bressan, J. D. and Williams, J. A. (1983). The use of a shear instability criterion to predict local necking in sheet metal deformation. International Journal of Mechanical Sciences 25(3): 155-168.
[38] Cockcroft, M. G. and Latham, D. J. (1968). Ductility and the workability of metals. Journal of the Institute of Metals 96: 33-39.
[39] Tvergaard, V. (1981). Influence of voids on shear band instabilities under plane strain conditions. International Journal of Fracture 17(4): 389-407.
[40] Gruben, G., Morin, D., Langseth, M. and Hopperstad, O. S. (2017). Strain localization and ductile fracture in advanced high-strength steel sheets. European Journal of Mechanics - A/Solids 61: 315-329.